DATA REPOSITORY: Appendix DR1 - Methodology

We synthesize rock uplift along the San Andreas fault (SAF) corridor using exhumation rates and topography. Exhumation rates are estimated from previously published low-temperature cooling-age data. Data include 257 apatite fission track (AFT) and/or (U-Th)/He (AHe) ages, which represent all published low-temperature cooling ages from samples that fall within 40 km of the trace of the SAF. All ages, along with sources, are presented in Table DR-1. AFT and AHe ages have closure temperatures of roughly 100º and 70ºC, respectively, although exact closure temperature varies based on cooling history and grainsize (Naeser, 1979; Gleadow and Duddy, 1981; Wolf et al., 1996; Farley, 2000). Cooling ages can be interpreted roughly as the time the sample cooled below the closure temperature, or the time since the sample exhumed through the depth at which that temperature occurs (closure depth, below the topographic surface). Closure depths assuming a 10ºC ambient surface temperature and 30ºC/km geothermal gradient, which are appropriate for the SAF corridor (Wright, 1987; Lachenbruch et al., 1985; Sass et al., 1992), are 3.2 and 2.0 km for AFT and AHe ages, respectively. We use these assumed depths to calculate an exhumation rate (E) for each cooling age (Table DR-1).

These estimates of exhumation rate are approximate, and ignore several factors that might be locally important. First, the cooling-age approach to calculating exhumation rate inherently assumes that samples were exhumed at an average rate since they became closed, which is not likely true in all cases. For this reason, our estimates of exhumation rate should be considered time-averaged. Second, we do not take into account local variations in heat flow, or the local effect of topography or advection (due to rapid exhumation) on isotherm shape (and hence, closure depths). This is a useful approximation, given the magnitude of the data used in our analysis and the case-specific data required for correcting for these factors, and the simplification should not affect the general trends we are testing for. Athough geothermal gradient does vary at greater distances to the fault (>50 km; Zoback et al., 2002), it is relatively uniform within the fault corridor. In fact, the SAF heat-flow anomaly has long been recognized as a broad region of elevated heat flow, as opposed to the spike in heat flow along the fault trace expected for a high-friction fault. In addition, the short-wavelength topography and moderate exhumation rates in the SAF corridor should not significantly affect closure depths due to topography or advection (Spotila et al., 2001). Nonetheless, the closure depths and calculated time-averaged exhumation rates should be viewed as having uncertainties of at least several tens of per cent.

Note that the use of cooling ages to estimate exhumation rates is inherently susceptible to variations where age-elevation gradients have developed in the crust due to steady-exhumation or time spent in partial annealing (AFT) or partial retention (AHe) zones (Gleadow and Duddy, 1981; Farley, 2000). This is illustrated in Figure DR-1, in which a reverse fault has tilted a mountain block to expose an age-elevation gradient with old ages (i.e. slow exhumation) at the highest elevation and young, reset ages (i.e. rapid exhumation) near the base. Time-averaged exhumation rates are calculated for each hypothetical age, showing how one location in close proximity to a fault can have a large variation in estimated exhumation rate. This may explain some of the variability in exhumation along the SAF, including the observation that slow rates of exhumation (rock uplift) are ubiquitous along the fault (Figure 2). For this reason, it is useful to highlight the maximum exhumation (rock uplift) rate at a given location, as illustrated by the envelopes in Figures 2a and 3a.

To obtain the time-averaged rock uplift rates, we combine these estimates of exhumation rate with a very rough approximation of surface uplift rate. It is important to include some measure of surface uplift, given that in many areas along the SAF, erosion is limited and major components of recent surface uplift are evidenced by plateau formation (Spotila et al., 1998). For each location, a time-averaged surface uplift rate was calculated as the elevation of the thermochronometry sample divided by 30 Ma (the age of the SAF system). This rough estimate of surface uplift was then added to the time-averaged exhumation rate to produce the time-averaged rock uplift rate (*RU*), which is plotted in Figures 2 and 3 versus various parameters along the SAF and tabulated in Table DR-1.

Although sporadic data exist for surface uplift over different time scales along the SAF, such as from marine or fluvial terraces, these data are too localized to use in our whole-fault synthesis. It is also beyond the scope of our synthesis to evaluate complex geologic data sets from specific locations. This simplified approach to surface uplift rates also ignores case-specific uplift history, such as locations which may have begun uplifting more recently than 30 Ma (e.g. the San Bernardino Mountains; Spotila et al., 1998). It also does not take into account variations in the local age of the SAF system along its length due to migration of triple junctions. Thus, our approach is clearly a gross simplification. However, the estimate of surface uplift is in most cases less than one-fifth of the total estimated rock uplift rate, such that the majority of the input comes from the thermochronometry. Despite the simplifications, we believe this is a useful technique that provides at least a first-order limit on rock uplift rates for the purpose of examining the tectonics of transpression along the SAF.

A necessary simplification in our analysis is to disregard horizontal translation along the SAF itself. Areas of given exhumation or topographic history are necessarily moving along the fault at the local rate of strike-slip translation, which varies from 1-3.5 cm/yr. In some locations, topography or zones of exhumation may be laterally advected away from localized features where they initiated, such as restraining bends or fault intersections (e.g. Wakabayashi et al., 2004). To restore features back to the fault segment they were adjacent to at the time of uplift or exhumation, however, requires specific knowledge of uplift, exhumation, and slip rate history, which generally does not exist. In addition, it is generally not known what fraction of slip rate consists of motion of one side of a fault with respect to fault features themselves (i.e. restraining bends); slip-rate is relative only between adjacent sides of the fault. Given that the typical length scale of fault features (e.g. nearly linear segments) and mountain ranges along the fault is ~50 km or longer, and that it takes several million years or more to accumulate this displacement on the SAF, this simplification is reasonable approximation for most locations.

Plots of rock uplift rate versus obliquity and the normalized shortening rate versus obliquity (Figures 2b and 2e) leave out six rock uplift data points from the King Range along the northernmost tip of the SAF. These data are based on young AFT ages of Dumitru (1991). Rapid exhumation in the King Range is produced by some combination of slip transfer towards the Mendocino triple junction, dynamic rock uplift due to thermal upwelling at a window in the subducting slab, and local obliquity of the SAF as it bends to the west. Because of the complexity of this area, the uncertainty as to what these rock uplift rates represent as far as accommodating plate motion, as well as the inability to accurately measure the obliquity of plate motion along such a tightly-curved segment of the plate boundary, we have left these data points off of these figures.

In addition to rock uplift rate, Figure 2 shows synthesis of topographic trends along the SAF, based on analysis presented in Spotila et al. (in press). The distributions of mean elevation and slope along the length of the fault are used to further elicit trends in recent surface uplift as well as intensity of erosion along the fault corridor. Each plot represents a profile taken along a swath that is centered along the main trace of the SAF; the mean elevation swath is 80-km wide and the slope-swath is 20-km wide. Topographic calculations were made using 3-arc second USGS DEMs, which have an appropriate scale of measurement given the >1000 km fault length. These DEMs have cell sizes of ~81-85 m for California's latitudinal range, so that slope calculations using the ArcView algorithm are long-wavelength and representative of average-length hillslopes (but potentially underestimate local slope). Absolute values of slope reported here should not be compared with slopes from higher resolution DEMs. Each data point of mean elevation and slope represents a calculation made at an interval along the swath at a roving window spaced each 10 km. Where swath areas lie offshore, elevations of 0 meters and slopes of 0^{o} were assigned and used for calculating averages.

Figure 2e and 2f plot crustal shortening normalized for local interplate velocity and degree of slip partitioning, both of which require additional information on plate motion and local fault slip rates. Local plate motion is based on the regional Pacific-North America interplate velocity from DeMets et al. (1999), minus any far-field component of plate motion that is taken up outside of the SAF system, such as the Basin and Range (based on GPS measurements of Argus and Gordon, 2001). The local slip rate along the SAF zone is based on data synthesized by WGEP (1995, 1999) as well as later local studies of Titus et al. (2005) and McLaughlin and Sarna-Wojcicki (2004).

Figure 2e also plots estimates of shortening (S') based on calculations of rock uplift. Shortening is estimated for each data point (Table DR1), by ascribing that rate of rock uplift to the entire 80-km-wide SAF corridor and calculating the shortening required to volumetrically balance the uplift, assuming a crustal thickness of 30 km. Given that the highest rates of rock uplift are localized near the SAF, this approach provides a maximum estimate of shortening for the entire corridor based on those data points. Given that both exhumation and surface uplift are used in the estimate of rock uplift rate, this approach takes into account shortening accommodated both by erosional efflux and topographic growth. However, it does not take into account the increase in thickness required to isostatically grow topography by the estimated rate of surface uplift. Isostasy is not considered, because most of the ranges involved are so narrow (<50 km) as to be supported by the lithosphere rather than isostatically compensated, and because surface uplift is a small fraction of the total rock uplift rates used. If areas do exist in which surface uplift is occurring due to crustal thickening, the shortening rates required to produce the uplift would be greater.

Additional References

Argus, D.F., and Gordon, R.G., 2001, Present tectonic motion across the Coast Ranges and San Andreas system in central California, Geol. Soc. Amer. Bull., 113, 1580-1592.

Blythe, A.E., d'Alessio, M.A., and Burgmann, R., 2004, Constraining the exhumation and burial history of the SAFOD pilot hole with apatite fission track and (U-Th)/He thermochronometry, Geophys. Res. Lett., 31, L15S16.

Blythe, A.E., Burbank, D.W., Farley, K.A., and Fielding, E.J., 2000, Structural and topographic evolution of the central Transverse Ranges, California, from apatite fission-track, (U-Th)/He and digital elevation model analyses: Basin Research, 12, 97-114.

Burgmann, R., Arrowsmith, R., Dumitru, T., and McLaughlin, R., 1994, Rise and fall of the southern Santa Cruz Mountains, California, from fission tracks, geomorphology, and geology: J. Geophys. Res., 99, 20,181-20,202.

d'Alessio, M.A., Blythe, A.E., and Burgmann, R., 2003, No Frictional heat along the San Gabriel fault, California: Evidence from fission-track thermochronology, Geology, 31, 541-544.

DeMets, C., and Dixon, T.H., 1999, New kinematic models for Pacific-North America motion from 3 Ma to present, I: Evidence for steady motion and biases in the NUVEL-1A model, Geophys. Res. Lett., 26, 1921-1924.

Dumitru, T.A., 1989, Constraints on uplift in the Franciscan subduction complex from apatite fission track analysis: Tectonics, 8, 197-220.

Dumitru, T.A., 1991, Major Quaternary uplift along the northernmost San Andreas fault, King Range, northwestern California: Geology, 19, 526-529.

Farley, K.A., 2000, Helium diffusion from apatite: general behavior as illustrated by Durango fluorapatite: J. Geophys. Res., 105, 2903-2914.

Gleadow, A.J.W., Duddy, I.R., 1981, A natural long-term track annealing experiment for apatite: Nucl. Tracks, 5, 169-174.

House, M.A., Niemi, N., Farley, K.A., Ducea, M., 2000, Uplift of California Coast Ranges: helium age constraints on the accommodation of vertical motion along strike-slip faults: Geol. Soc. Amer. Abstr. with Prog., 32, A-242.

Lachenbruch, A.H., J.H. Sass, and S.P. Galanis Jr., 1985, Heat flow in southern California and the origin of the Salton Trough: J. Geophys. Res., 90, 6709-6736.

McLaughlin, R.J., and Sarna-Wojcicki, A.M., 2004, The right-releasing stepover between the Rodgers Creek-Healdsburg and Maacama fault zones; modeling the evolution of young pull-apart basins along the northern part of the east San Francisco Bay strike-slip fault system, U.S. Geol. Surv. Open-File Report, 1424, 61-69.

Naeser, C.W., 1979, Fission-track dating and geologic annealing of fission tracks: *in* E. Jager and J.C. Hunziker, eds., Lectures in Isotope Geology, pp.154-169, Springer-Verlag, New York.

Naeser, C.W., and Ross, D.C., 1976, Fission track ages of sphene and apatite of granitic rocks of the Salinian block, Coast Ranges, California: Jour. Res. U.S. Geol. Survey, 4, 415-420.

Sass, J.H., Lachenbruch, A.H., and Moses, T.H.Jr., 1992, Heat flow from a scientific research well at Cajon Pass, California: J. Geophys. Res., 97, 5017-5030.

Spotila, J.A., Farley, K.A., and Sieh, K., 1998, Uplift and erosion of the San Bernardino Mountains, associated with transpression along the San Andreas fault, CA, as constrained by radiogenic helium thermochronometry: Tectonics, 17, 360-378.

Spotila, J.A., Farley, K.A., Yule, J.D., and Reiners, P.W., 2001, Near-field transpressive deformation along the San Andreas fault zone in southern California, based on exhumation constrained by (U-Th)/He dating: J. Geophys. Res., 106, 30909-30922.

Titus, S.J., DeMets, C., and Tikoff, B., 2005, New slip rate estimates for the creeping segment of the San Andreas fault, California, Geology, 33, 205-208.

Wakabayashi, J., Hengesh, J.V., and Sawyer, T.L., 2004, Four-dimensional transform fault processes: Progressive evolution of step-overs and bends, Tectonophys., 392, 279-301.

WGEP (Working Group on California Earthquake Probabilities), 1995, Seismic hazards in southern California: Probable earthquakes, 1994-2024, Bull. Seism. Soc. Amer., 85, 379-439.

WGEP (Working Group on California Earthquake Probabilities), 1999, Earthquake probabilities in the San Francisco Bay region: 2000 to 2030 - A Summary of findings, U.S. Geol. Surv., Open File Report 99-517, 60 p.

White, L.A., 1992, Thermal and unroofing history of the western Transverse Ranges, California; results from apatite fission track thermochronology, Ph.D. Thesis: University of Texas, Austin, 299 p.

Wolf, R.A., K.A. Farley, Silver, L.T., 1996, Helium diffusion and low temperature thermochronometry of apatite: Geochimica Cosmochimica Acta, 60, 4231-4240.

Wolf, R.A., Farley, K.A., Silver, L.T., 1997, Assessment of (U-Th)/He thermochronometry: The low-temperature history of the San Jacinto Mountains, California, Geology, 25, 65-68.

Wright, T.L., 1987, Geologic evolution of the petroleum basins of southern California: *in* T.L. Wright and R. Heck, eds., Petroleum Geology of Coastal Southern California, Pacific Section, Am. Assoc. Petroleum Geologists, Los Angeles, California, 1-19.

Zoback, M.D., Townend, J., and Grollimund, B., 2002, Steady-state equilibrium and deformation of intraplate lithosphere, International Geology Review, 44, 383-401.

Figure and Table Captions

Table DR-1: Thermochronometry along the San Andreas fault corridor. All published AFT and AHe ages known to the authors from samples located within 40 km of the trace of the San Andreas fault are listed here. Samples are numbered sequentially in order from north to south, but identified using the original published sample name (*Sample ID*). Sources (*Ref.*) are as follows: 1 = Naeser and Ross (1976); 2 = Dumitru (1989); 3 = Burgmann et al. (1994); 4 = White (1992); 5 = Spotila et al. (1998); 6 = Spotila et al. (2001); 7 = Blythe et al. (2000); 8 = Spotila et al. (in press); 9 = Dumitru (1991); 11 = Wolf et al. (1996); 12 = Buscher and Spotila (in press); 13 = d'Alessio et al. (2003); 14 = Niemi et al. (in prep.); 15 = Blythe et al. (2004); 16 = S. Kelly (unpublished data). Only two surface samples used from Blythe et al. (2004), no samples from the Parkfield borehole itself. Only the oldest and youngest AFT ages of 17 samples from one location from d'Alessio et al. (2003) were used. Location of samples are given as *D1* (distance along-strike on the San Andreas fault, measured from 0 km starting in the south at Bombay Beach) and *D2* (fault-normal distance between the sample location and the trace of the San Andreas fault), both in km. Latitude and longitude of samples are available in the published sources. The local obliquity of the San Andreas fault to plate motion is given as the angle α, in degrees. Elevation at the sample site is given as *Elev.*, in meters. Apatite fission track (*AFT*) and apatite (U-Th)/He ages (*AHe*) are given in Ma. Exhumation rate (*E*) is given in mm/yr based on AFT and AHe ages are calculated assuming a 3.2 km closure depth for AFT, and 2.0 km closure depth for AHe (see text for more explanation). Rock uplift rate (*RU*) is given in mm/yr as the sum of the exhumation rate and a component of surface uplift, where surface uplift is defined as the sample's elevation divided by 30 Ma (see text for more explanation).

Table-DR2: Slip partitioning data along the San Andreas fault, used for Figure 2f. Location of each calculation is given as distance in km along the San Andreas fault, measured from south to north (*Distance*). Slip rate along individual faults or fault segments are given for each location in mm/yr, with fault's abbreviated as SAF (San Andreas fault), SJF (San Jacinto fault), EF (Elsinore fault), SCF (San Clemente fault), ECSZ (Eastern California shear zone), PVF (Palos Verdes fault), NIF (Newport-

Inglewood fault), BPF (Big Pine fault), WWF (White-Wolf fault), OF (Ozena fault), SJnF (San Juan fault), RF (Rinconada fault), CF (Calaveras fault), SGF (San Gregorio fault), HF (Hayward fault), GF (Greenville fault), CGF (Concord-Green Valley fault), RCF (Rodgers Creek fault), and MF (Maacama fault). Slip rate (*U*) along adjacent fault segments are added (*Sum*), and divided by the plate motion at that location (*D*) to yield the degree of partitioning (*U*/*D*). Plate motion is based on DeMets et al. (1999), minus the motion accommodated in the Basin and Range (north of distance = 305 km) (based on GPS measurements of Argus and Gordon, 2001). The local plate motion obliquity is given as α (in degrees). Sources for slip-rate data are from WGEP (1995; 1999), Titus et al. (2005), and McLaughlin and Sarna-Wojcicki (2004).

Figure-DR1: Hypothetical cross section illustrating the architecture of cooling age isochrons that can result from uplift along a fault. Isochrons for a single thermochronometric technique are shown as dashed lines. Uplift along the reverse fault has tilted the "stratigraphy" of isochrons, such that the oldest ages occur at the highest elevation and at the greatest distance from the fault, and the youngest ages occur right at the fault itself. Time-averaged exhumation rates for each isochron are illustrated. Note how much variation in exhumation rate exists in one location that is very proximal to the fault. This variation is an artifact of the method used to calculate time-averaged exhumation, as the rock uplift rate along the fault zone has been constant and does not vary with distance from the fault in this example. This artifact may help explain some of the variation in exhumation rate along the SAF, such as the observation that slow rates are present everywhere along the fault (including in the near-field).

Table DR1: Thermochronometry along the San Andreas fault corridor.

#	Sample ID	Ref.	D1 (km)	D2 (km)	α	Elev. (m)	AFT (Ma)	AHe (Ma)	E (mm/yr)	RU (mm/yr)
1	8997-23	9	1103	9.2	4.6	380	50.1		0.06	0.08
2	8997-7	9	1102	1.4	4.6	115	0.3		10.53	10.54
3	8997-8	9	1102	0.8	4.6	240	0.9		3.51	3.52
4	8997-9	9	1102	2.6	4.6	25	12.0		0.26	0.26
5	8997-6	9	1102	2.7	4.6	15	12.4		0.25	0.26
6	8997-15	9	1101	1.9	4.6	700	1.5		2.11	2.13
7	8997-4	9	1101	3.2	4.6	5	13.3		0.24	0.24
8	8997-20	9	1101	3.6	4.6	565	1.7		1.86	1.88
9	8997-21	9	1101	6.8	4.6	300	40.3		0.08	0.09
10	8797-32	9	1101	0.8	4.6	400	1.6		1.98	1.99
11	8997-31	9	1101	2.6	4.6	5	12.1		0.26	0.26
12	8997-14	9	1100	1.5	4.6	615	3.2		0.99	1.01
13	8797-33	9	1100	0.4	4.6	625	0.5		6.32	6.34
14	8997-13	9	1100	1.2	4.6	525	60.3		0.05	0.07
15	8997-12	9	1100	1.0	4.6	600	1.1		2.87	2.89
16	8997-3	9	1100	3.0	4.6	5	12.7		0.25	0.25
17	8997-2	9	1100	2.1	4.6	0	8.8		0.36	0.36
18	8997-1	9	1099	1.4	4.6	5	1.7		1.86	1.86
19	8997-18	9	1099	5.1	4.6	360	25.0		0.13	0.14
20	8997-16	9	1098	2.6	4.6	665	1.4		2.26	2.28
21	8697-142	2	1052	17.3	-22.8	22	27.8		0.11	0.11
22	8697-141	2	1051	27.0	-22.8	518	24.8		0.13	0.14
23	8697-140	2	1046	31.1	-22.8	609	33.5		0.09	0.11
24	8697-139	2	1044	38.3	-22.9	608	46.9		0.07	0.09
25	DR-510	1	880	1.2	-2.2	129	68.4		0.05	0.05
26	DR-521	1	864	1.6	-2.3	11	60.9		0.05	0.05
27	DR-532A	1	847	16.6	-2.5	60	59.6		0.05	0.06
28	DR-975	1	822	36.8	-3.7	30	14.8		0.21	0.21
29	F1	2	801	12.9	-3.9	20	43.1		0.07	0.07
30	DR-1	1	778	6.0	0.9	299	23.1		0.14	0.15
31	Leo-126	1	727	14.7	11.5	720	17.5		0.18	0.20
32	K13-87	3	712	5.0	11.4	366	61.2		0.05	0.06
33	BL-6-88	3	711	5.3	11.4	360	67.3		0.05	0.06
34	85-010	2	711	31.5	11.4	658	75.9		0.04	0.06
35	RR-17	3	709	1.8	11.4	770	3.6		0.88	0.90
36	RR-15	3	708	2.6	11.4	880	5.2		0.61	0.64
37	RR-10	3	708	3.7	11.4	1000	4.9		0.64	0.68
38	RR-13	3	708	3.3	11.4	1020	5.1		0.62	0.65
39	RR-12	3	708	3.6	11.4	1030	2.0		1.58	1.61
40	RR-2	3	708	4.9	11.4	990	7.0		0.45	0.48
41	86-052	2	669	37.5	12.0	378	59.6		0.05	0.07
42	DR-1127A	1	664	3.5	12.0	396	49.6		0.06	0.08
43	DR-1354	1	655	4.8	11.9	632	45.7		0.07	0.09
44	DR-1455	1	650	13.1	11.9	6	2.8		1.13	1.13
45	Gab3	8	649	5.0	9.9	768		35	0.06	0.08
46	Gab1, 2	8	648	4.1	9.9	707		18.7	0.11	0.13
47	Gab5	8	646	2.8	9.8	537		13.1	0.15	0.17
48	Gab6	8	645	2.5	9.8	476		16.3	0.12	0.14
49	Gab7, 8	8	645	1.5	9.8	277		24	0.08	0.09
50	DR-566C	1	629	8.3	2.7	621	16.7		0.19	0.21
51	DR-844	1	619	16.6	2.6	443	24.2		0.13	0.15
52	DR-1748B	1	617	36.8	2.6	1128	39.5		0.08	0.12
53	DR-847A	1	616	17.0	2.6	169	22.1		0.14	0.15
54	DR-573	1	593	13.3	2.4	201	40.6		0.08	0.08
55	multi	15	533	1.0	6.9	700		32	0.06	0.09
56	BARN	15	529	3.0	6.9	750	60.2		0.05	0.08
57	SLO-5B	1	492	40.9	1.6	457	70.1		0.05	0.06
58	TS-1	1	489	34.7	1.5	494	71.0		0.04	0.06
59	BM4-90	4	480	25.7	1.5	262	56.3		0.06	0.06
60	BM3-90	4	479	28.8	1.5	1036	60.1		0.05	0.09
61	TOR12-87	4	479	34.0	1.5	573	65.3		0.05	0.07
62	TOR9-87	4	477	34.9	1.5	500	65.9		0.05	0.06
63	TOR13-87	4	477	36.5	1.5	451	48.0		0.07	0.08
64	TOR6-87	4	477	38.3	1.5	427	53.0		0.06	0.07
65	TOR5-87	4	476	39.4	1.4	427	69.9		0.05	0.06
66	Black 1	8	476	28.9	1.4	798		9.2	0.22	0.24
67	BM1-90	4	475	30.9	1.4	622	46.9		0.07	0.09
68	BM2-90	4	475	28.7	1.4	829	57.3		0.06	0.08
69	Black 2	8	474	26.3	1.4	613		8.4	0.24	0.26

#	Sample ID	Ref.	D1 (km)	D2 (km)	α	Elev. (m)	AFT (Ma)	AHe (Ma)	E (mm/yr)	RU (mm/yr)
70	Black 3	8	474	26.3	1.4	491		12.3	0.16	0.18
71	TOR4-87	4	472	38.7	1.4	433	53.5		0.06	0.07
72	TOR14-87	4	472	41.0	1.4	658	52.9		0.06	0.08
73	TOR3-87	4	472	39.7	1.4	512	62.6		0.05	0.07
74	TOR2-87	4	472	40.7	1.4	555	63.0		0.05	0.07
75	P-11	1	469	23.9	1.4	600	17.3		0.18	0.20
76	LaP-4D	1	468	21.4	1.4	592	62.6		0.05	0.07
77	CR9-90	4	413	7.5	8.9	814	37.6		0.08	0.11
78	CR8-90	4	411	8.0	8.9	853	38.0		0.08	0.11
79	CR7-90	4	411	9.0	8.9	884	43.8		0.07	0.10
80	CR6-90	4	409	8.6	8.9	927	44.9		0.07	0.10
81	CR5-90	4	398	4.0	8.8	951	60.2		0.05	0.08
82	CR4-90	4	398	4.1	8.8	963	53.0		0.06	0.09
83	CR3-90	4	397	5.3	8.8	994	66.9		0.05	0.08
84	CR2-90	4	397	6.2	8.8	866	42.1		0.08	0.10
85	CR1-90	4	393	4.3	8.8	884	36.0		0.09	0.12
86	SBC2-87	4	388	18.4	12.7	975	17.9		0.18	0.21
87	SBC1-87	4	388	21.8	12.7	951	26.6		0.12	0.15
88	SBC3-87	4	388	22.5	12.7	1097	25.8		0.12	0.16
89	SBC4-87	4	387	22.7	12.7	1067	25.0		0.13	0.16
90	SBC7-87	4	386	23.9	12.7	1012	19.5		0.16	0.20
91	SBC13-87	4	385	24.0	12.7	1042	24.7		0.13	0.16
92	SBC12-87	4	385	24.8	12.7	1067	27.6		0.11	0.15
93	SBC10-87	4	384	25.7	12.7	1097	28.0		0.11	0.15
94	SBC9-87	4	383	25.4	12.7	1103	25.0		0.13	0.16
95	SBC36-90	4	382	25.7	12.7	1122	16.8		0.19	0.23
96	SBC35-90	4	382	26.6	12.7	1140	29.9		0.11	0.14
97	SBC34-90	4	382	27.6	12.7	1183	45.9		0.07	0.11
98	SBC32-90	4	382	28.7	12.7	1268	47.1		0.07	0.11
99	SBC31-90	4	382	29.3	12.7	1305	66.3		0.05	0.09
100	SBC41-90	4	380	28.9	19.6	1268	54.1		0.06	0.10
101	SBC42-90	4	379	29.6	19.6	1122	51.0		0.06	0.10
102	CG6-90	4	369	29.0	27.6	1341	44.5		0.07	0.12
103	CG2-90	4	368	30.9	27.5	1387	40.0		0.08	0.13
104	CG1-90	4	368	28.4	27.5	1539	55.5		0.06	0.11
105	CG5-90	4	368	30.5	27.5	1311	47.5		0.07	0.11
106	CG4-90	4	367	30.4	27.5	1356	21.9		0.14	0.19
107	DK4-89	16	364	8.0	37.5	912	17.9		0.18	0.21
108	DK8-89	16	363	5.7	37.5	1019	12.7		0.25	0.28
109	DK6-89	16	363	5.9	37.5	976	18.7		0.17	0.20
110	DK11-89	16	362	4.7	37.5	1069	17.0		0.19	0.22
111	DK10-89	16	362	4.7	37.5	1050	13.9		0.23	0.26
112	NNSE5	14	361	4.3	37.5	1100		6.7	0.30	0.34
113	NNSE4	14	361	3.7	37.5	1179		4.4	0.45	0.49
114	NNSE3	14	360	2.3	37.5	1287		5.2	0.38	0.43
115	NNSE2	14	359	1.0	37.5	1402		4.4	0.45	0.50
116	PLC7-89	16	356	5.6	37.4	1129	13.5		0.23	0.27
117	PLC8-89	16	356	5.5	37.4	1134	10.8		0.29	0.33
118	PLC3-89	16	355	7.3	37.4	976	19.9		0.16	0.19
119	PC51-87	4	358	27.3	37.5	1341	2.8		1.13	1.17
120	PC52-87	4	358	28.7	37.5	1143	4.3		0.73	0.77
121	Pinos5	8	356	4.9	37.5	2537		21.9	0.09	0.18
122	Pinos4	8	355	5.0	37.4	2402		27	0.07	0.15
123	PC10-87	4	354	22.7	37.4	1494	43.1		0.07	0.12
124	Pinos3	8	354	4.5	37.4	2244		22.9	0.09	0.16
125	Pinos1	8	354	1.5	37.4	1903		37.7	0.05	0.12
126	Pinos6	8	354	3.7	37.4	2049		21.7	0.09	0.16
127	PC25-87	4	354	23.4	37.4	1987	27.1		0.12	0.18
128	Pinos2	8	353	3.8	37.4	2049		23.2	0.09	0.15
129	PC9-87	4	353	22.3	37.4	1484	50.6		0.06	0.11
130	NNSC1	14	353	0.7	37.4	1873	1873.0	5.1	0.39	0.45
131	PC7-87	4	351	22.1	37.4	1463	50.5		0.06	0.11
132	PC6-87	4	351	21.0	37.4	1469	57.2		0.06	0.10
133	PC3-87	4	350	19.5	37.4	1433	42.8		0.07	0.12
134	PC20-87	4	350	19.5	37.4	1433	24.5		0.13	0.18
135	PC2-87	4	350	19.0	37.4	1448	57.0		0.06	0.10
136	PC43-90	4	349	18.0	37.4	1402	52.3		0.06	0.11
137	PC42-90	4	348	16.9	37.4	1387	64.6		0.05	0.10
138	Emig1	8	348	0.8	37.4	1646		4.2	0.48	0.53
139	PC41-90	4	347	15.8	37.4	1341	61.6		0.05	0.10
140	TG1	14	346	1.2	37.4	1933		7.5	0.27	0.33

#	Sample ID	Ref.	D1 (km)	D2 (km)	α	Elev. (m)	AFT (Ma)	AHe (Ma)	E (mm/yr)	RU (mm/yr)
141	TG2	14	346	1.0	37.4	1790		8.7	0.23	0.29
142	TG3	14	345	0.6	37.4	1628		5.7	0.35	0.41
143	NNGR1	14	345	9.5	37.4	1241		55.6	0.04	0.08
144	TG8	14	342	10.1	37.3	695		59	0.03	0.06
145	NNGR6	14	341	5.2	37.3	1522		12.6	0.16	0.21
146	SEGR9	14	341	1.3	37.3	1420		7.9	0.25	0.30
147	NNGR5	14	341	4.3	37.3	1595		12.9	0.16	0.21
148	TG7	14	341	7.8	37.3	974		38.5	0.05	0.08
149	TG5	14	340	3.7	37.3	1428		11.7	0.17	0.22
150	SEGR10	14	340	2.0	37.3	1651		9.6	0.21	0.26
151	LL4	12	318	2.9	34.1	1278		27.5	0.07	0.12
152	JBSG10	12	309	2.7	29.1	1735		11.6	0.17	0.23
153	LL5	12	308	0.8	29.1	1101		10.6	0.19	0.23
154	JBSG9	12	308	3.8	29.0	1362		8.3	0.24	0.29
155	JBSG7	12	305	3.6	29.0	1749		32.8	0.06	0.12
156	JBSG11	12	302	4.9	29.0	1257		22.9	0.09	0.13
157	JBSG14	12	301	10.7	29.0	630		7	0.29	0.31
158	JBSG6	12	301	0.9	29.0	1464		10.5	0.19	0.24
159	JBSG13	12	300	11.3	29.0	608		10.4	0.19	0.21
160	LL7	12	298	5.7	29.0	800		4.6	0.43	0.46
161	LL6	12	293	0.5	28.9	1104		13.4	0.15	0.19
162	JBSG15	12	290	2.2	28.9	1184		8.4	0.24	0.28
163	LL1	12	289	1.7	28.9	1020		15.8	0.13	0.16
164	JBSG2	12	286	6.1	28.9	1340		5.2	0.38	0.43
165	JBSG1	12	285	5.9	28.9	1230		5.6	0.36	0.40
166	LL2	12	285	5.8	24.9	1005		5.4	0.37	0.40
167	JBSG5	12	279	3.7	24.8	1077		4.2	0.48	0.51
168	oldest of 17	13	273	30.8	24.8	671	73.5		0.04	0.07
169	youngest of 17	13	273	30.8	24.8	671	27.3		0.12	0.14
170	SG29	7	270	19.6	24.7	650	27.9		0.11	0.13
171	SG19	7	267	33.6	24.7	520	59.5	42.4	0.05	0.06
172	SG28	7	267	16.8	24.7	700	42.1		0.08	0.10
173	SG3	7	262	34.3	24.7	470	47.7	33.3	0.06	0.08
174	SG4	7	260	32.2	24.7	530	51.2	34.6	0.06	0.08
175	SG26	7	258	20.3	24.6	1680	51.2		0.06	0.12
176	SG27	7	255	10.5	24.6	1220	37.1	23.2	0.09	0.13
177	SG5	7	255	31.5	24.6	560	6.1		0.52	0.54
178	SG20	7	253	27.3	24.6	990	16.1		0.20	0.23
179	SG6	7	252	30.1	24.6	670	10.0	3.1	0.65	0.67
180	SG24	7	251	21.7	24.6	1070	63.6		0.05	0.09
181	SG25	7	247	16.8	24.5	1280	38.3		0.08	0.13
182	SG21	7	245	23.5	24.5	1170	48.4		0.07	0.10
183	SG23	7	241	18.2	24.5	1620	43.6	42.8	0.05	0.10
184	SG2	7	240	36.4	24.5	350	26.7		0.12	0.13
185	SG7	7	239	30.1	20.5	1710	11.9	7.6	0.26	0.32
186	SG22	7	238	23.8	20.5	1520	36.3		0.09	0.14
187	SG38	7	238	12.6	20.5	2140	40.9	40.6	0.05	0.12
188	SG1	7	235	33.6	20.4	270	11.8	6.6	0.30	0.31
189	SG37	7	231	9.1	20.4	2050	14.2		0.22	0.29
190	SG33	7	229	14.0	20.4	1700	19.3	8.9	0.22	0.28
191	SG8	7	226	32.9	28.4	230	5.3	6.3	0.32	0.33
192	TableMtn2a	8	225	4.0	28.4	1381		19.2	0.10	0.15
193	SG9	7	225	29.4	28.4	350	3.0		1.05	1.07
194	SG10	7	224	27.3	28.4	419	4.5		0.70	0.72
195	SG36	7	221	2.7	20.3	2100	3.7		0.85	0.92
196	SG30	7	221	20.1	20.3	500	9.0		0.35	0.37
197	TableMtn1a	8	219	0.5	20.3	2008		10.4	0.19	0.26
198	SG31	7	218	20.7	20.3	820	13.0	6.8	0.29	0.32
199	SG14	7	215	26.6	20.3	470	40.4		0.08	0.09
200	SG35	7	215	1.4	20.3	2150	8.6		0.37	0.44
201	SG12	7	211	7.0	20.2	3070	7.0	5.1	0.39	0.49
202	SG11	7	207	16.8	20.2	980	8.4		0.38	0.41
203	SG42	8	207	7.7	20.2	2019		1.8	1.11	1.18
204	MH99TP3a	8	207	7.5	20.2	2380		6.8	0.29	0.37
205	SG40	8	207	6.3	20.2	2383		6	0.33	0.41
206	MH99TP2a	8	205	9.1	20.2	2657		5.7	0.35	0.44
207	MH99TP1	8	205	9.8	20.2	2131		10.9	0.18	0.25
208	99MHCP3	8	204	11.2	20.2	2620		5.2	0.38	0.47
209	99MHCP1	8	204	11.5	20.2	2533		5.4	0.37	0.45
210	SG39	7	196	11.5	20.1	1022	32.7		0.10	0.13
211	SB1	7	196	4.2	20.1	980	53.6		0.06	0.09

#	Sample ID	Ref.	D1 (km)	D2 (km)	α	Elev. (m)	AFT (Ma)	AHe (Ma)	E (mm/yr)	RU (mm/yr)
212	SG17	7	195	6.4	14.1	840	42.3		0.07	0.10
213	SB2	7	193	7.8	14.1	1130	56.8		0.06	0.09
214	SG16	7	190	6.1	14.1	700	18.2		0.17	0.20
215	SB3	7	184	10.1	14.0	1050	60.2		0.05	0.09
216	SB4	7	178	8.4	21.0	1200	54.9		0.06	0.10
217	SB5	7	177	17.9	21.0	1390	57.1		0.06	0.10
218	SBHe10	5	175	17.8	20.9	1329		51.2	0.04	0.08
219	SB22	7	169	6.8	20.9	1080	57.4		0.06	0.09
220	SB7	7	159	11.2	28.8	1875	58.2		0.05	0.12
221	SBHe19	5	156	0.7	28.8	652		0.7	2.86	2.88
222	SB8	7	156	14.5	28.8	2130	54.4		0.06	0.13
223	SBHe17	5	156	16.1	28.8	2113		64.3	0.03	0.10
224	SBHe20	5	155	4.9	28.8	756		18.2	0.11	0.14
225	SBHe16	5	154	15.2	28.8	1812		52.4	0.04	0.10
226	SBHe15	5	154	14.5	28.8	1614		49.4	0.04	0.09
227	SBHe7	5	152	12.7	28.8	1233		20.6	0.10	0.14
228	SB9	7	150	21.5	28.7	2070	90.9		0.03	0.10
229	SBHe26	5	147	5.7	29.7	1899		14.5	0.14	0.20
230	SBHe25	5	145	11.9	29.7	1861		40.8	0.05	0.11
231	SBHe23	6	144	4.5	29.7	1387		1.4	1.43	1.47
232	DYJS5	6	144	2.4	29.7	1506		1.4	1.43	1.48
233	DYJS4	6	144	2.6	29.7	1658		1.4	1.43	1.48
234	SB11	7	143	34.0	29.7	1550	70.4		0.04	0.10
235	DYJS3	6	143	3.0	29.7	1768		1.4	1.43	1.49
236	SBHe22	6	143	2.0	29.7	1969		1.6	1.25	1.32
237	DYJS2	6	143	3.4	29.7	1908		1.6	1.25	1.31
238	DYJS1	6	142	3.8	29.7	2060		1.5	1.33	1.40
239	SBHe21	6	142	2.2	29.7	2323		1.5	1.33	1.41
240	SBHe24	5	140	9.5	29.7	3311		52.6	0.04	0.15
241	SB10	7	140	30.9	29.7	1970	45.5		0.07	0.14
243	SBHe12	5	138	5.6	7.6	1526		14.3	0.14	0.19
244	SBHe27	5	133	9.5	7.6	3506		55.7	0.04	0.15
245	DYJS6	6	120	4.1	43.5	981		5.2	0.38	0.42
246	TP	11	120	11.6	43.5	1275		52.5	0.04	0.08
247	DYJS7	6	117	6.6	43.5	1333		4.5	0.44	0.49
248	XL, CL	11	112	10.5	43.4	2070		50.5	0.04	0.11
249	FR	11	111	12.4	43.4	2575		55.7	0.04	0.12
250	KW	11	109	26.3	43.4	1420		39.6	0.05	0.10
251	SC	11	108	7.2	43.4	430		30	0.07	0.08
253	DYJS9	6	106	2.3	43.4	556		12.6	0.16	0.18
254	SJP	11	103	15.0	26.4	3290		79.2	0.03	0.13
255	UT	11	98	13.7	26.3	2605		35	0.06	0.14
256	JS	11	96	33.8	26.3	1530		67	0.03	0.08
257	PS	11	92	10.5	17.3	150		17.1	0.12	0.12

Table DR2: Partitioning data along the San Andreas fault.

Distance, km	SAF	SJF	EF	SCF	ECSZ	PVF	NIF	BPF	WWF	OF	SJnF	RF	CF	SGF	HF	GF	CGF	RCF	MF	Sum	U/D	α
5	25	12	2.5																	39.5	0.79	6.5
55	25	12	2.5																	39.5	0.79	4
105	25	12	2.5	1.5	8															49	0.98	26.3
155	25	12	2.5		8	3	1.5													52	1.04	29.6
205	35		2.5		10	3	1.5													52	1.04	20.1
255	35				10															45	0.9	24.5
305	35				10															45	0.9	28.9
355	35							1	1											37	0.95	37.3
405	35									2										37	0.95	8.8
455	35										2									37	0.95	2.3
505	35											2								37	0.95	1.7
555	35											2								37	0.95	7.2
605	30											2								32	0.82	2.5
655	30																			30	0.77	11.9
705	17.4												15	3						35.4	0.91	11.3
755	17.4												15	3						35.4	0.91	5.7
805	17.4												6	7	9	2				41.4	1.06	-3.9
855	24														9	2	5			40	1.03	-2.5
905	24																	9		33	0.85	2.9
955	24																		10	34	0.87	0.4
1005	24																		8	32	0.82	-6.2
1055	24																		7	31	0.79	-22.7
1105	24																		7	31	0.79	-14.3

Figure DR-1

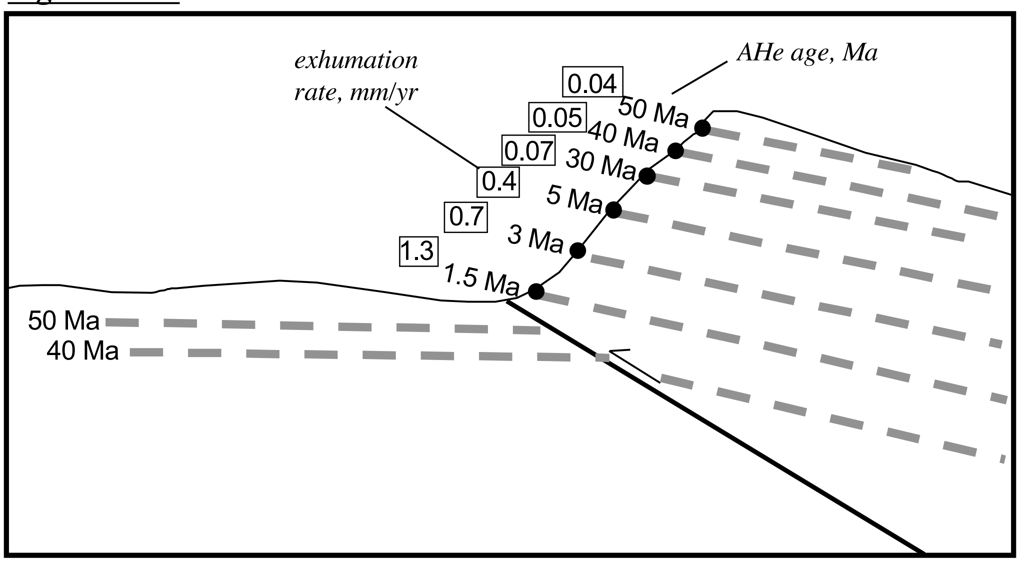
exhumation
rate, mm/yr
AHe age, Ma
0.04
0.05
0.07
0.4
0.7
1.3
50 Ma
40 Ma
30 Ma
5 Ma
3 Ma
1.5 Ma
50 Ma
40 Ma